PHYSICAL REVIEW A, VOLUME 61, 033804

Computational investigation of the Ni-like Gd collisionally pumped x-ray laser

S. McCabe and G. J. Pert
Physics Department, University of York, Heslington, York YO10 5DD, United Kingdom

(Received 4 May 1999; published 11 February 2000)

The Ni-like Gd X-ray laser is investigated in detail primarily through a 1.5-dimensional combined fluid and atomic physics code EHYBRID. Directly measurable parameters are calculated using a combined optical ray-tracing and saturation calculation code RAYTRACE. As experimental data for Gd are not widely available, we compare the predictions of our model with experimental results for Sm. There has been considerable success reproducing the results of experiment with this model. Much has been made of the similarities between the operating conditions for Ne- and Ni-like lasers. This approach has been quite successful from an experimental viewpoint. In this paper we consider the degree of similarity. Areas of difference are highlighted particularly the relative stability of the lasant ion stages.

PACS number(s): 42.55.Vc, 82.20.Wt, 42.60.By

I. INTRODUCTION

In recent years the focus of work in collisionally pumped x-ray lasers has shifted away from Ne-like schemes toward shorter wavelength Ni-like schemes. The application of techniques used to enhance the output of Ne-like lasers has led to rapid progress in Ni-like x-ray laser development. Reported lasing wavelengths have rapidly shortened, and a saturated operation is claimed for Sn and Sm lasers. The Ne-like scheme, in particular the Germanium laser, has been thoroughly investigated [1] and is well understood. More than a decade ago the first cross-section calculations appeared for the Ni-like Gd scheme [2] with lasing predicted for the $3d^9 4d_{3/2}(J=0) \rightarrow 3d^9 4p_{3/2}(J=1)$ and $3d^9 4d_{3/2}(J=0) \rightarrow 3d^9 4p_{1/2}(J=1)$ transitions at 61 and 66 Å, respectively, as a result of the large excitation cross section from the ground state to the upper lasing level. This was shortly followed by a detailed local thermodynamic equilibrium model [3]. Little detailed theoretical or computational work has been published in the intervening years. The simulations presented here are based on a 112-level model of the Gd Ni-like ion stage using the calculations of Hagelstein [2]. This model includes detailed calculations of the collision rates on excited transitions [4]. Results quoted in this paper are for the 66-Å lasing line. This transition has the larger oscillator strength in Gd. A 253-level model with detailed calculations for ground-state transitions [5] in conjunction with the van Regemorter approximation [6] for optically allowed transitions between excited levels was also investigated. The second model produced significantly different results despite excellent agreement between the two sets of collision rates. Different fitting functions used for Hagelstien's data [4,7] and the data of van wyngaarden *et al.* [8] indicated a possible source for divergence at low electron energies but these are well below the minimum energy at which any significant Ni-like population is generated in the plasma. The cause of the deviation is a direct result of the inaccuracy of the van Regemorter approximation. This is dealt with in more detail below.

A combined hydrodynamic and atomic physics code (EHYBRID) developed at York by Pert [9] has been used extensively and successfully in the prediction of experimental observables for Ne-like Ge. We validate the code for Ni-like schemes by comparing the calculated output energies, and more particularly the predicted trends with the results of Sm x-ray laser experiments for which there is a significant volume of experimental data. This comparison is subject to some limitations. A three-dimensional raytracing code RAYTRACE [10] is used to generate experimental observables. This code was originally designed for long pump pulse 1-ns experiments, and assumes a plasma varying slowly with respect to the x-ray transit time, i.e., the plasma is assumed static within the RAYTRACE code. This limits the codes accuracy when calculating x-ray laser output parameters, where the gain changes significantly on time scales less than the transit time of the targets used. For the 14-mm targets used as the basis of our experimental comparison in Sec. VI, the transit time is approximately 50 ps. The time during which gain is greater than 80% of maximum from simulation is of the order of 20 ps, significantly less than the transit time. This problem is not addressed in this paper, but it should be noted that there is a project underway to address this problem explicitly. The static plasma implies that the RAYTRACE code will correctly model a traveling-wave experiment but will increasingly overestimate the output of a laser as the gain time reduces below the transit time for the target.

In this paper we concentrate on the dual 100-ps pumping scheme that is the current workhorse of the x-ray laser community. The potential of very short ($\lesssim 1$ ps) pulses in conjunction with longer pulses (>100 ps) for collisional excitation [11,12] is also examined. Very short high-intensity pump pulses produce rapidly ionizing plasmas with potentially high gains for short times. Such pumping schemes are commonly referred to as transient collisional excitation (TCE) schemes. Estimations of the relative gains achievable are made. Recently there have been a number of successful Ni-like experiments [13] using this scheme.

A zero-dimensional (0D) version of the full EHYBRID code is used to compare the operation of the Ne-like Ge and Ni-like Gd schemes. This is used to highlight the areas of difference between the two schemes, often overlooked in the preparation of experiments. In particular the problem of overionization is examined. This problem has been noted before in computational studies [14] and in experiment [7].

II. COMPUTER MODELS

The principle code used is EHYBRID, a 1.5-dimensional (1.5D) two-fluid code designed to operate in planar geometry. The major axis of the fluid expansion is modeled in the plane of the driving laser with a Lagrangian mesh [15,9]. The laser beam is assumed to have a Gaussian profile at the target surface with a variable full width at half maximum (FWHM) independent of the target size. Electron-ion thermalization and flux-limited electronic and ionic thermal conduction ($f=0.1$) are included. Laser absorption via inverse bremsstrahlung is the primary absorption mechanism with a fractional dump at the critical density. The dump primarily acts to initiate the plasma with only a small fraction of the incoming laser beam reaching the critical density region under normal operating conditions. In addition, a full raytrace of the incoming laser beam may be switched on to model the effects of refraction in the plume. Radiative losses are included through bremsstrahlung, photorecombination, and line emission.

The atomic kinetics of the Ni-like ion are modeled using a collisional-radiative model [16]. Two separate sets of data are used with 112 [4] and 253 [5] excited levels. These data include all transitions from the $3d$ ground state and from states originating from $3s$ and $3p$ holes to the $n=4$ manifold, and from $n=4$ and 5 manifolds, respectively. Excited states of higher principal quantum number are grouped to reduce computation time. For the 112-level model, collision rate information is available for the excited states of the $n=4$ manifold. For the 253-level model the van Regemorter approximation is used. The validity of this approximation is limited [17], and will be addressed later in the paper. Collision cross sections on optically forbidden transitions between the excited states are not available. It is assumed that optically allowed transitions will dominate in determining the excited level mixing at least within the $n=4$ manifold.

Other ion stages are modeled in various ways depending on available data and the significance of the ion stage. Data for Gd includes detailed descriptions of the Cu-like ion and averaged level descriptions of Co- and Zn-like ion stages. For Sm we use a screened hydrogenic model to calculate the averaged excited states for ion stages close to Ni-like. These levels are scaled using exact calculations of the ionization energy from the multiconfiguration Dirac-Fock method [18]. Other ion species are modeled through a detailed mechanistic model derived from the model of Griem [19] described in detail by Dave [20].

The RAYTRACE code postprocesses the EHYBRID output data to generate experimental observables such as near and far field laser profiles, output energies, and refraction angles. The code is fully 3D using the self similar lateral expansion of EHYBRID directly. The plasma is assumed to be uniform along the lasing axis. The ramifications of this assumption with regard to experimental optimization have been mentioned briefly in Sec. I and are discussed in detail in Sec. V.

III. 0D MODEL FINDINGS

To systematically investigate the temperature and density space of the plasma and the operation of the Ni-like scheme, we first used a 0D code. This code is a subset of EHYBRID running in a single cell with the hydrodynamics routines switched off and no electron-ion thermalization. The full collisional-radiative model is used. The electron and ion temperatures and the ion density are all fixed. The output is therefore the response of the system to an electron temperature step function. The ion temperature was set independently in these simulations to 150 eV. This temperature is representative of those achieved in the full hydrodynamic simulation. We use this temperature to more accurately reflect the gains achieved in full simulations.

Identical simulations were performed for Ge and Gd. Ge and Gd are superficially similar. The upper lasing levels are 1337 and 1340 eV, and the ionization energies for the Ne-like and Ni-like ion stages are 2192 and 2630 eV, respectively. This makes them ideal candidates for a comparative computational study. The data presented for each element consist of a figure containing three contour plots labeled (a), (b), and (c). Plot (a) shows the average ionization of the plasma when the system has reached a steady state. Plot (b) shows the gain calculated in this steady state. Plot (c) is the peak gain achieved while the plasma is ionizing. This final plot provides an indication of the gain enhancement achievable in transient pumping or TCE schemes.

We will start by examining the germanium results shown in Fig. 1. Figure 1(a) is similar to Fig. 3 of Holden *et al.* [1]. We include dielectronic recombination and use a more detailed model of the Ne-like ionization stage, but otherwise the code is identical. The inclusion of dielectronic recombination increases the relative population of Ne-like ions in the equilibrium plasma, and this is reflected in the slower rise of average ionization predicted in our 0D calculations. This is consistent with Fig. 6 from the same paper. Figure 1(b) shows the gain in the steady state with the ionization balance included. Many previous calculations have assumed all ions to be Ne-like. This indicates an optimum electron temperature of 500 eV at an electron density of 10^{21} cm^{-3} with a peak gain <20. On the other hand, Fig. 1(c) shows the peak gain achieved while the system was ionizing. This shifts the optimum conditions to higher temperatures and slightly higher electron density, but also indicates that much higher gains may be achieved in this regime. This result is a good indication of the enhancement that can be achieved in moving to TCE schemes.

The conclusions drawn for Ge by Holden *et al.* [1] may be repeated here. It is clear that the optimum gain conditions do not coincide with those conditions which produce a suitable steady-state ionization balance. The laser functions typically at electron temperatures $\sim 400 \rightarrow 900$ eV, and in the upper limit of this range the ion is stripped in steady state to a dominant species of N-like ions, Ne-like ions forming only a fraction of a percent of the plasma.

Figure 2 contains the results of identical calculations for Gadolinium using a 112-level data set. The primary conclusions drawn for Ge are equally valid here. The most striking difference is the relative instability of the Ni-like ionization stage. The contour plot [Fig. 2(a)] for average ionization as a function of temperature and density shows this clearly. The relevant ion stages of interest are Ne-like Ge ($Z=22$) and

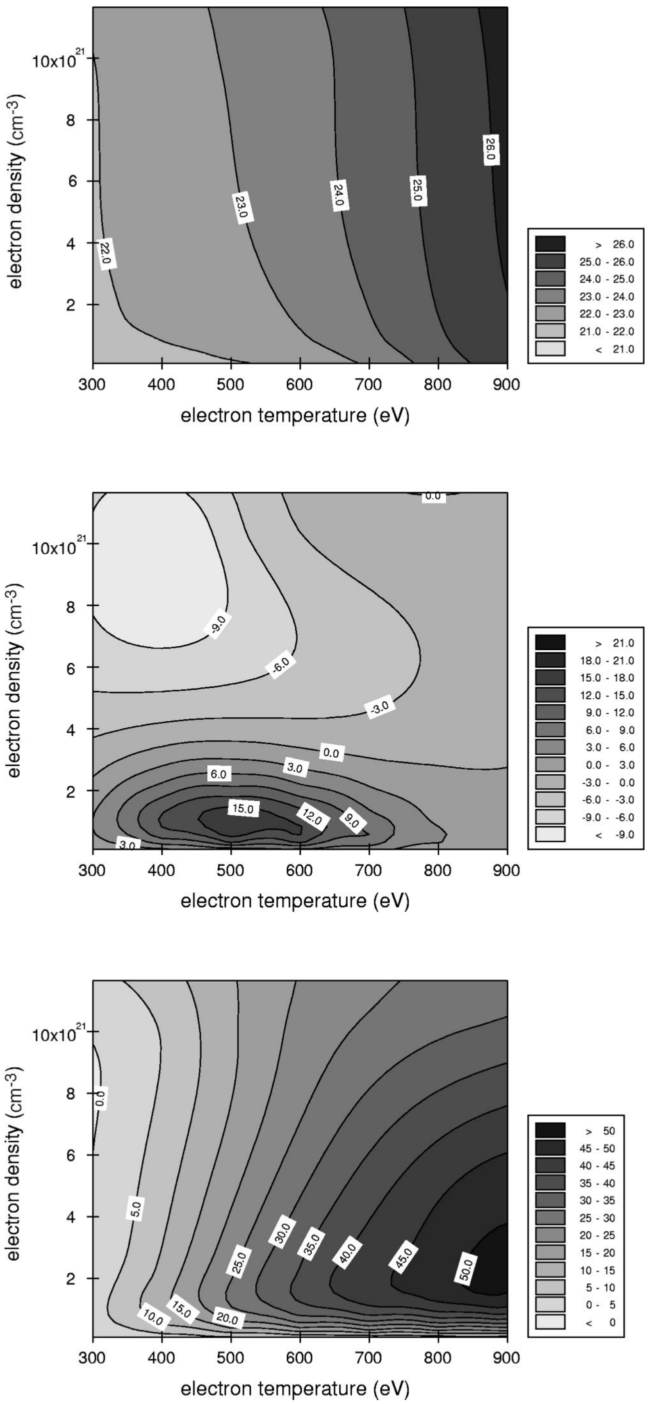

FIG. 1. Contour plots generated by the germanium 0D calculations. The ion temperature is set to 150 eV. From the top, the plots show the following: (a) steady-state ionization and balance average ionization, (b) equilibrium gain (cm^{-1}), and (c) peak transient gain (cm^{-1}).

Ni-like Gd ($Z=36$). Contour lines indicating an average ionization of 22 and 36 traverse almost identical paths in the temperature density plot. Following lines of equal electron density, Gd reaches a Co-like average ionization after an average temperature increase of 50 eV. Ge is significantly more stable, requiring a 200-eV rise in electron temperature to increase the average ionization by one. The relatively rapid sweep through the Ni-like stage is emphasized by the steady-state gain calculations [Fig. 2(b)]. This indicates that a significant Ni-like Gd population occupies a much smaller region of the parameter space investigated. These data underline the Ne-like Ge conclusion that the conditions for a steady-state ionization balance dominated by Ni-like ions is significantly different from the conditions required for optimum gain. The peak gain plot for the ionizing plasma [Fig.

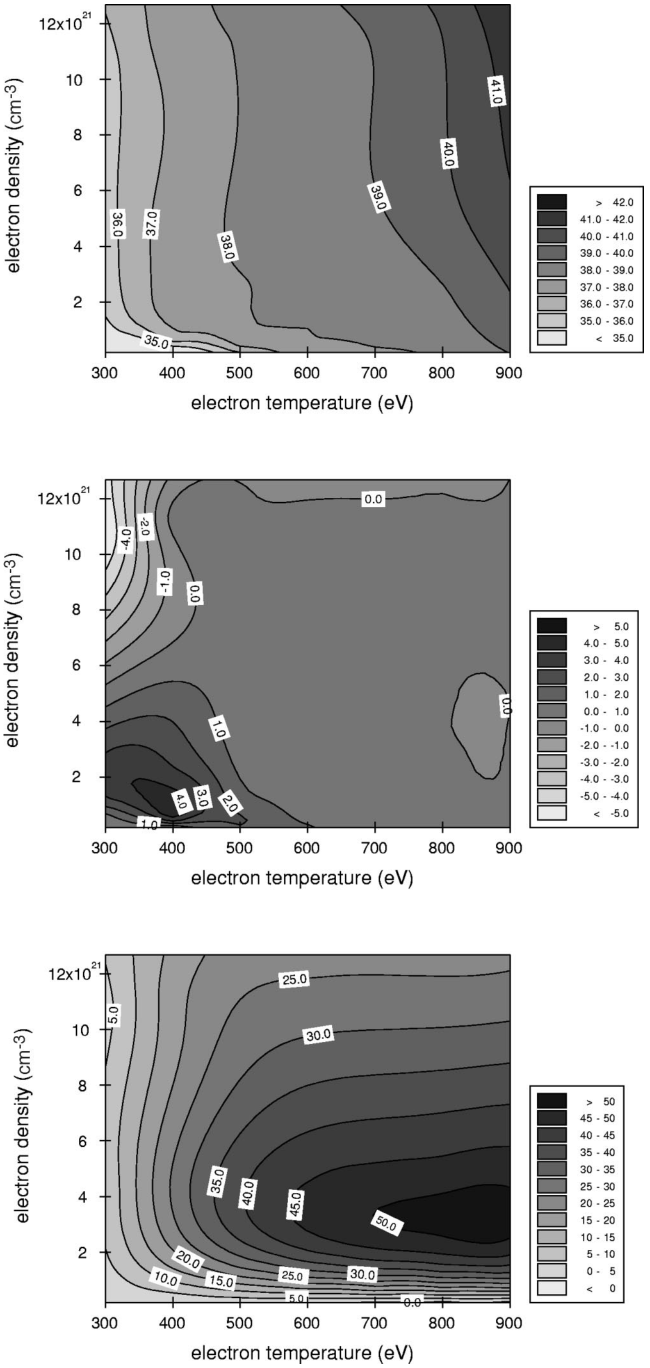

FIG. 2. Contour plots generated by the gadolinium 0D calculations. The ion temperature is set to 150 eV. From the top, the plots show the following: (a) steady-state ionization and balance average ionization, (b) equilibrium gain (cm^{-1}), and (c) peak transient gain (cm^{-1}).

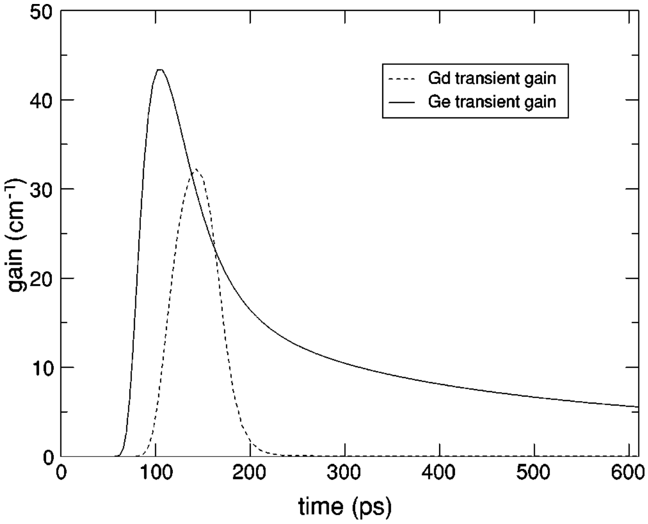

FIG. 3. A sample plot of the temporal evolution of gain from the steady-state calculations. The electron temperature is 800 eV and the electron density is 10^{21} cm^{-3}.

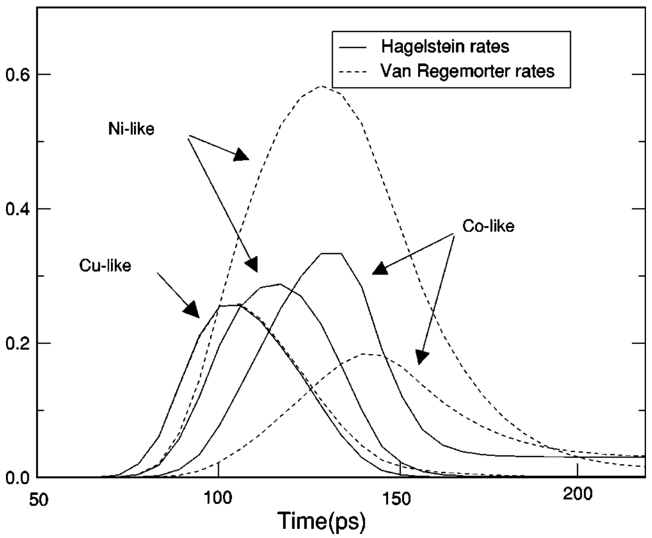

FIG. 4. The effect of using the van Regemorter approximation for the Ni-like ion stage is shown using a plot of the time evolution of the populations of the Ni-like and bounding ion stages.

2(c)] is an accurate indicator of the conditions required for lasing. Furthermore, it is clear that this is a transient gain condition and that the peak gain occurs long before the steady state is reached. It must also be noted that dielectronic recombination is not a significant contributor to the gain of Ni-like Gd. Full 1.5D simulations were also performed, with the dielectronic recombination contribution to the Ni-like ion stage removed with much less than 1% change in gain.

The relative instability of the Ni-like ion stage is a result of the larger collision cross section of excited states having a higher principal quantum number compared to the Ne-like scheme for the lasing levels. The monopole excitation rate into the upper lasing level of Gd is greater than twice that of the Ge upper lasing level. The large electron impact cross sections increase stepwise excitation through the $n=4$ and higher manifolds, adding significantly to the ionization rate. The increased ionization is very significant for the stability of the lasant ion stage. As a result the Ni-like ion stage burns through very rapidly, leading to overionization in a very short time. The large area of zero gain in Fig. 2(b) indicates that the Ni-like stage population is insignificant at electron temperatures greater than 550 eV in the steady state.

The peak transient gain is less affected by the overionization problem. A contour plot of gain as a function of electron density and temperature [Fig. 2(c)] indicates a usable parameter space not disimilar to Ne-like Ge shown in Fig. 1(c). The predicted gains are also similar in magnitude. This is a reflection of the higher pumping rate into the upper lasing level maintaining gain despite the smaller Ni-like ion population. As expected, the temporal evolution of the gain in Gd is faster reflecting the rapid ionization rate. Using as an example an electron density of 10^{21} cm^{-3}, and an electron temperature of 800 eV the temporal FWHM of the Gd gain profile is half that of Ge (see Fig. 3). It can also be seen that the Gd gain returns to zero, indicating that at this temperature the Ni-like ion stage is depleted in the steady state. In contrast, Ne-like Ge is not fully depleted at this temperature. The extent of the overionization is detailed in Fig. 2(a) above. The higher excitation rate compensates for relatively lower lasant ion populations as a result of ‘‘overionization.’’ The rapid rise in peak gain as a function of temperature reflects the larger excitation rate.

A 253-level model based entirely on the published data of Zhang *et al.* [5] was also implemented. Results from this model are not included as the implementation relied on the use of the van Regemorter approximation to provide excitation rates between excited states of the lasant manifold. Deviations between the calculated excitation rates and the van Regemorter approximation were found to be large. The majority of rates were significantly underestimated, some by more than an order or magnitude, while others were overestimated by 20% or more. This meant that no simple correction could be made to the van Regemorter approximation. This has been discussed in some detail by Sampson and Zhang [17], and they recommend discontinuing use of the approximation. The effect of using van Regemorter rates for the $n=4$ manifold when compared with the calculated rates is shown in Fig. 4. The graph shows the relative populations of the major ion stages present as a function of time for a 0D calculation, i.e., as the system approaches steady state. All ion stages except Ni-like stages are treated identically. The van Regemorter rates slow the ionization to such an extent that the peak Ni-like population is more than doubled and has a longer lifetime. Use of the approximate rates in conjunction with the data set of Zhang *et al.* significantly increases the relative Ni-like population and gain. This is completely due to the approximation, as the calculated collision rates from the ground state are almost identical (within 5%) to those used in the 112-level model. The gain is overestimated by more than the relative population difference in the two cases. Pumping into the upper lasing level from the ground is the same in both cases, whereas the collisional depopulation rate into other states is significantly underestimated by the approximation. An imbalance between ground-and excited-state populations is introduced by mixing the rates.

IV. 1.5D SIMULATION RESULTS

We have carried out a significant number of full simulations, using the codes to determine optimum pumping parameters and examine the conditions required to deliver maximum output energy. We have concentrated in this paper on the two 100-ps pulse scheme shown to be the most efficient of the long pulse configurations. The operation of the double-pulse pumping technique is well known. The first pulse (or prepulse) is used to generate a long scale length plasma. This reduces refraction effects and increases the laser source size. The second pulse is then used to pump the plasma to sufficiently high temperatures for lasing. The timing of the second pulse and the relative power of the prepulse are variables in a large parameter space. To keep the analysis simple, we will examine a small number of simulations and indicate the critical areas to monitor when optimizing such a scheme.

The simulations are run within the following constraints to minimize the parameter space and ensure that they are relevant to experiments performed on the VULCAN laser system at Rutherford Appleton Labs. The maximum energy in a single pulse is 60 J for 70–100-ps pulses into a 2-cm line focus. The simulations performed relate to an experiment using 14-mm targets, and the total energy on target is scaled accordingly. The prepulse fraction is arbitrarily limited to between 1% and 33% of the main pulse maximum energy. We limit the prepulse fraction, as its contribution at other energies can be inferred from the data.

Before discussing the results of the complete set of simulations and how they compare with experimental results, we will discuss further the role of the prepulse. Figure 5 shows the expansion of a Gd target driven by 0.4-, 2-, and 13-J prepulses over a period of 7 ns. Radial expansion is measured from the target back surface. This explains the 20-μm offset of the radial expansion axis. The contour plot represents the calculated fractional energy dump from a laser pump into the plasma plume as a function of time. Superimposed on the contour plots are the regions of significant absorption for a laser pump pulse. We define the region of significant absorption as the region in which 90% of the pulse energy would be absorbed. The smallest prepulse, plot (a), barely starts the expansion process. The preplasma has an initial maximum electron temperature of 25 eV and an average ionization of less than 15. As this layer expands away from the surface it cools and recombines, and the ion density drops. The electron density of the expanding plume rapidly becomes too small ($\approx 10^{18}\ \mathrm{cm}^{-3}$), more than 100 μm from the surface for significant inverse bremsstrahlung absorption. Therefore, a second laser pulse will be absorbed in a layer that remains close to the target surface. This region has very low ionization (≈ 4) and temperature (≈ 6 eV), but this is offset by a high ion mass density between 0.1% and 1% that of solid suitable for collisional pumping. To generate a good signal the radial extent of the region needs to be of the order of 50 μm to produce a reasonable source size. This explains the long optimal pulse separations obtained in experiments at low prepulse levels. The requirement that the plume electron density reach an optimal low gradient is replaced by a need for the region behind the plume to become large enough to support a reasonable source size. It should be noted at this stage, as will be mentioned again in Sec. VI, that the accuracy of simulations is reduced at such low prepulse levels.

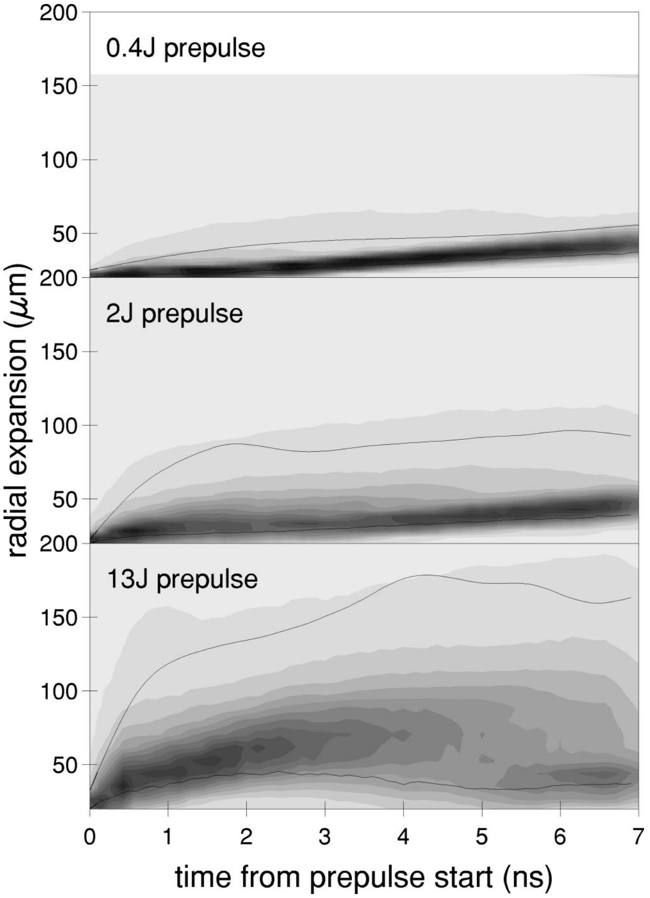

FIG. 5. Evolution of the plasma and corresponding absorption region. The shading indicates where laser energy would be absorbed at the onset of a driving pulse. The bounding lines indicate the region in which 90% of the laser energy would be absorbed. Three different prepulses are shown for comparison.

For larger prepulses optimized conditions occur when the inital high-density layer has expanded and cooled sufficiently to form a large enough low-density gradient region to minimize refraction and maximize the source area. As this region continues to expand the electron density will decrease until it is relatively transparent to the pump pulse. At this point the expansion behind the plume will absorb most of the pump energy. This process can be seen in plot (c) for the 13-J prepulse. Initially a very hot rapidly expanding plasma is generated (300 eV, average ionization 33). The hot plasma expands and cools, and within the first 3 ns a large region of uniform absorption is created. After this time the rapid expansion and cooling reduce the electron density such that pump pulse energy is being dissipated over a larger volume such that the local temperatures produced are reduced and

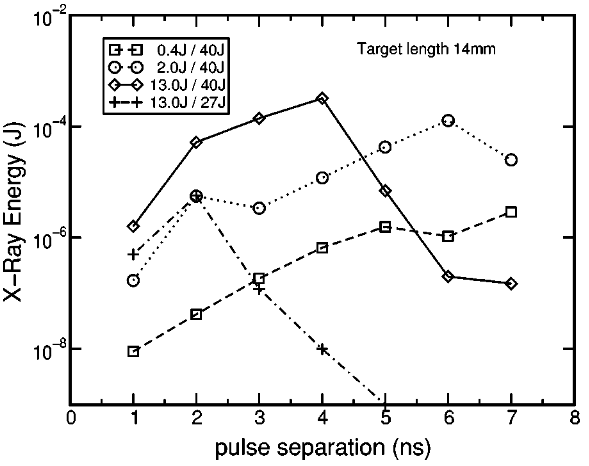

FIG. 6. Gadolinium dual 100-ps pulse optimization curves for a 14-mm target. Four different main and prepulse configurations are contrasted.

laser gain is reduced. It must be noted that in both cases the optimized second pulse arrival time is a function of the energy of the pulse. The smaller the pulse the earlier it must arrive to achieve optimum lasing; otherwise the density at the energy dump will drop below the critical level required for lasing. The 2-J prepulse is not large enough to detach the absorption region from the surface as the 13-J prepulse does; however, it produces a much larger and initially more uniform absorption region than the 1% prepulse. The results below show that this level of prepulse was the optimum for the conditions considered.

Figure 6 is a pulse separation optimization scan for 1%, 5%, and 33% prepulse levels equal to pulse energies of 0.4, 2, and 13 J on target, respectively. The total energy in all cases is different, but for low prepulse levels this factor is not significant. Experimental fluctuations would easily mask the difference. For the larger 13-J prepulse, the prepulse is a significant portion of the total energy available. We have also run simulations for this prepulse level with the main pulse reduced to keep the total energy constant. A target length of 14 mm is used for these simulations. The data clearly indicate that the optimum pulse separation increases with decreasing prepulse level. This is what we predict from an examination of the data in Fig. 5. It also predicts that for a specified main pulse energy increasing the prepulse energy will increase the laser output within the bounds of the simulation. The situation is more complex when we take into account a fixed total energy, where increasing the prepulse level reduces the energy of the main pulse. We show the significance of this effect, including an optimization curve for a 13-J prepulse, where the total energy is the same as for the 2-J prepulse. This adds another prepulse level measurement to our parameter space, as this is a 48% prepulse. Optimized timings are not simply a function of prepulse percentage or indeed prepulse energy. They are more complex, occupying a parameter space that may be presented and analyzed in the form of a contour plot of energy against prepulse and main pulse energies.

We feel that the reference to prepulse levels as fractions is something of a red herring in experimental optimization curves. There are two reasons for this. First, it is often more informative to know the total energy deposited per shot in addition to the prepulse level. Second, in an experiment the total energy on a shot-to-shot basis can vary such that 5% and 10% prepulse levels can form a continuum of prepulse energies. It would be more informative to plot the energy as a continuous variable rather than as a discrete prepulse percentage. This is not so important in simulations where conditions are fixed, but again it is more informative to refer to pulse energies rather than ratios.

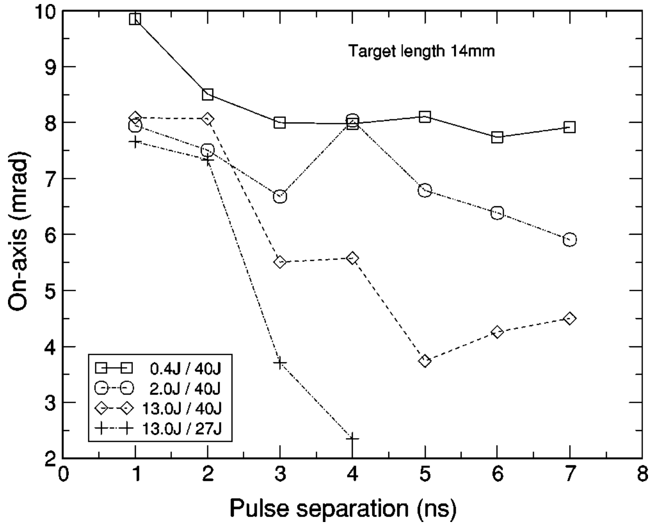

FIG. 7. Gadolinium dual 100-ps pulse output laser on axis refraction angle for a 14-mm target. Four different main and prepulse configurations, as in Fig. 6, are contrasted.

Plotting the x-ray laser beam refraction angles (Fig. 7), increases our understanding of the optimization curves of Fig. 6. For smaller pulse separations the plasma scale length is small. Gain occurs in a highly refracting region of the plasma close to the surface, as implied by the absorption plots. The rapid expansion of the higher-energy prepulses and the consequent electron-density gradient reduction in the absorbing region results in a significant drop in refraction angle at 3 ns. In comparison, the smallest prepulse simulated does not exhibit such a drop in refraction angle. There are two 13-J prepulse simulations using 40- and 27-J main pulses. For the 40-J main pulse, the refraction angle begins to increase after 5 ns. This corresponds to a change in the energy deposition profile, a consequence of the rapid expansion and reduction in the electron density of the preplasma. At this time absorption initially occurs in a region of high electron-density gradient close to the target surface; see Fig. 5. Refraction is higher for the larger main pulse because this pulse generates its own local density gradients over the time scale of the pulse. These gradients are related to the degree of heating, and the larger main pulse is refracted to a greater degree.

The length of the pulse is also important. The same energy delivered in a shorter time can produce higher gains. In simulations, for a 2-J prepulse, where the main pulse time has been reduced to a 50-ps FWHM, an increase in gain is found. This increase can be attributed to larger pumping rates due to the generation of hotter electrons by the higher intensity pump. The approximate temperature peaks during the main pulses are 900 and 1040 eV for the 100- and 50-ps pulses, respectively. Further reducing the pulse width is the basis of the TCE schemes. Shorter high-intensity pulses generate much hotter electrons, pumping all levels much harder, in particular those with larger monopole excitation rates such as the upper lasing level in Ni-like Gd. To make the TCE scheme work we must replace the single main pulse with two pulses. A short pulse alone is not sufficient. The reason for this is that the main pulse in the two-pulse experiment has a dual role: first to heat the expanding and cooling plasma to the correct ionization stage, and second to pump the upper lasing level. The TCE schemes break this process into two separate stages using two pulses: a longer low-intensity pulse and a very short high-intensity pulse.

Using the shorter 50-ps main pulse, x-ray laser refraction is slightly increased from 7 to 8 mrad. This is primarily a function of the first stage of the two-stage process described above. The time required to heat the plasma to the lasant ion stage causes a delay of 40 ps between the start of the pumping pulse and the onset of lasing. The more rapid energy dump into the plasma generates a larger electron density gradient over the x-ray laser source region. To minimize this, the energy must be deposited very rapidly into a region where the electron density gradient is small and, ideally, the majority of ions would be in the ground state of the lasant stage. This concept underlies the TCE scheme, but the scheme is made more complex by the need to pump the plasma into the correct ion stage prior to the short pump pulse. We do not intend to cover this scheme in detail in this paper; however, it should be noted that TCE experiments using pulses of the order of 1 ps for Ne- and Ni-like schemes indicate that a prepulse is not always required for optimal lasing [21]. A recent publication from our group [14] also indicates that a prepulse is not always advantageous in a dual long-pulse–short-pulse experiment. In this paper optimal lasing was achieved with a single long pulse and 2-ps coherent-potential-approximation pulse for the 62 Å inner-shell transition of Ne-like germanium.

V. SIMULATION VERSUS EXPERIMENT

In this paper we have concentrated on Ni-like Gd, as we have the most complete set of data for this element. Unfortunately there is very little experimental data for this element. The reason for this is most likely related to difficulties involved in target preparation. We will compare the predictions of our code with experimental results for Sm reported by Lin *et al.* [22]. We expect the elements Gd and Sm to behave similarly as they have $Z=64$ and 62, and Ni-like ionization energies of 2630 and 2370 eV, respectively. We will show that we can predict the behavior and trends of Ni-like x-ray lasers under different pumping configurations.

In predicting experimental observables we must consider the influence of factors not included in the model. It is important to have some understanding of how the simplifications used influence the simulation results. Significant experimental factors not included are (i) beam irregularities (the beam being assumed to be uniform along the target, and Gaussian transversely), and (ii) the precise pump beam geometry (multiple beams are combined in the experiment; they do not all strike the target normally as assumed in the simulation). We may infer that the effect of local irregularities in the beam intensity at the focal plane will lead to small-scale plasma disturbances in the transverse direction. The creation of a nonuniform plasma with local hot and cold spots implies local mismatches between the gain regions. The effect of nonuniformities in the plasma would depend on their exact configuration; however, we assume that they would enhance output only in exceptional circumstances. In general the effect would be to flatten optimization curves, as an experimental plasma constitutes a mix of simulated pulse energies, each having different optimum temporal pulse separations. The influence of beam geometry is less clear; however, there is already a large correction to the absorbed energy, 0.5, based on the results of long pulse ($\approx 1\ \mu$m) experiments carried out using the same geometry [1,23]. Including these factors would destroy the symmetry of the system and add greatly to the complexity of the model. Their inclusion would not greatly enhance our understanding of the underlying system.

In addition to these considerations the RAYTRACE code will overestimate the signal where the gain times are shorter than the transit time of the target. Some work has been done to account for this by other users of the code [24]. No correction has yet been incorporated into the original code. In current simulations the temporal FWHM of the gain is 30 ps, and the 80% gain time less than 20 ps, both significantly less than the transit time of the targets. An underestimation of gain and output signal is unavoidable due to the higher ionization energy of Ni-like Gd compared to Ni-like Sm. This may be as much as a factor of 2 as reported by Daido *et al.* [7]. Taking all of these effects into consideration, it is expected that output energies from simulation will overestimate experimental values due to the dominance of the assumptions inherent in the RAYTRACE code.

We compare our simulations with the results of an experiment to optimize the dual pulse pumping configuration for Ni-like Sm at Rutherford Appleton Laboratories in the UK [22]. The general results of the experiment indicate the following. For smaller prepulses the temporal pulse separation required to achieve the maximum signal increases. Prepulse ratios of less than 1% can produce significant output signal. The output signal range is from 1 nJ to 3 μJ. Our simulations agree with the general thrust of the observations. The observation of larger pulse separations being optimum for smaller pulse ratios, implying smaller prepulse energies, is obeyed. We predict larger output signals, but this is expected as outlined above. The only significant discrepancy between our simulations and the data presented is the output for very small prepulses.

A direct comparison between experimental and simulated data is shown in Fig. 8. This shows the significant areas of agreement. The peak signal is overestimated by a factor of 4, while the optimum pulse ratio predicted is in error by a similar amount. The exact experimental parameters are used in the code. Taking into account the complexity of the experi-

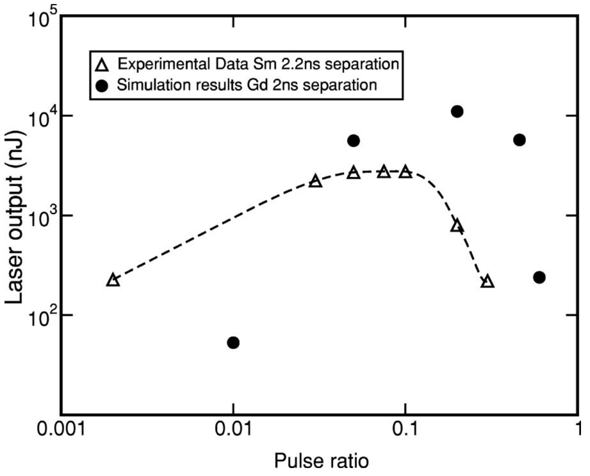

FIG. 8. Experimental data from Lin *et al.* compared to predictions of the EHYBRID fluid and atomic code postprocessed with the RAYTRACE code. X-ray laser output energies are compared.

ment and simulation, we consider this level of agreement to be very good.

The one area of concern is the prediction of simulations at low prepulse levels corresponding to total prepulse energies of less than 1 J. Simulations with such small prepulse ratios (≈1% or less) at the experimental total energies do not produce significant plasma plumes. Using computationally expensive equation-of-state packages has not shed much light on this, and there is little variation from results using the ideal gas equation approximation. To give the correct plasma energies and ionization balance, the experimental laser input energies have been divided by 2, as mentioned above. This correction may not be applicable at lower incident energies, and may be different for prepulse and mainpulse energies. We have no experimental data on the prepulse temperatures to validate this hypothesis. Including this factor would still not explain the low output energies for a 0.01% prepulse. It may be possible that a very small pedestal pulse is present in the experimental system; however, this has not been reported.

A comparison of experimental and simulated refraction angles is shown in Fig. 9. The trend of simulated refraction angles agree with experiment; however, the absolute angles are larger by 2 mrad for comparable configurations. Part of the reason for this is that we plot the on-axis refraction maxima rather than the radial refraction angle of the peak signal. The on-axis refraction maximum is greater than the radial refraction for a maximum signal by between 1 and 2 mrad. However, this value is not as accurately known as the raw data from the raytrace has a coarse grid. This is illustrated by the far field contour plot (Fig. 10). The shape of the far-field plot shown is dominated by the axial symmetry of the simulated plasma. A much smoother version of this profile is observed in experiment. We feel that the level of agreement between experiment and the experimental observables produced by the codes on the basis of these results is very good, taking into account the uncertainties discussed above.

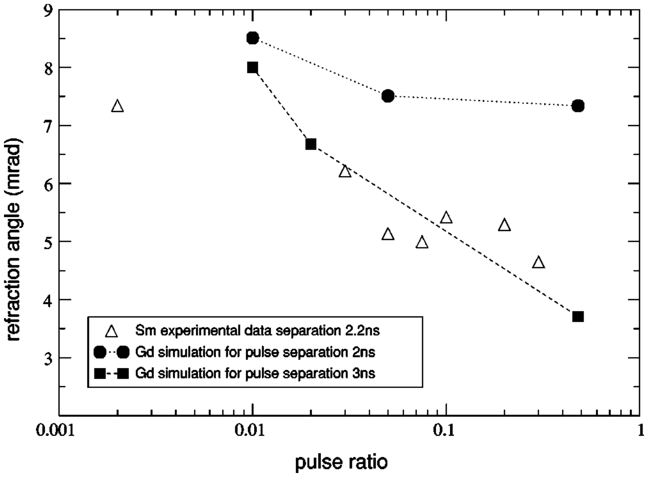

FIG. 9. Experimental data from Lin *et al.* compared to predictions of the EHYBRID fluid and atomic code postprocessed with the RAYTRACE code. X-ray laser refraction angles are compared.

VI. CONCLUSION

The complexity of the laser plasma interaction and the prediction of x-ray laser output parameters based on that interaction is very sensitive to a number of factors. It is important that the atomic data be as accurate and complete as possible for the lasant level. Use of approximations can lead to large unforseen errors, as we have shown for the van Regemorter approximation. Less obviously, factors such as the laser-pulse shape can influence the outcome. We conclude this from the results of the pulse width simulation, which shows how the rate of energy supplied to the plasma influences the electron temperature. In general, it is apparent that for smaller prepulses a longer time separation is required to maximize the output signal. However, the optimum time depends on the prepulse energy and main pulse energies

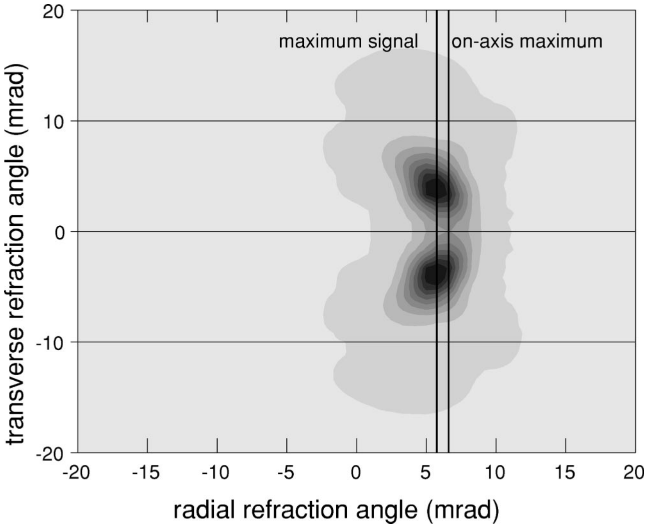

FIG. 10. Farfield output from RAYTRACE for 2 and 40 J at 4 ns on a 14-mm target. Note the refraction angle marked on the axis calculated from the raw data, and the estimated refraction angle calculated from the plot.

separately. The ratios of the two pulses should not be considered to define the optimum, but should only be used as a shorthand after the energies have been clearly defined.

We have shown that while Ne- and Ni-like schemes have similar operating conditions, there are a number of differences that are important to consider when transferring concepts from one to the other. The majority of optimization concepts have transferred well from Ne- to Ni-like systems: for example, the use of prepulses to increase the plasma scale length. The relative instability of the Ni-like stage, as shown in Sec. III, has a direct bearing on the operation of the systems, and care must be taken not to overionize Ni-like lasers.

We have shown in Sec. V that our codes reproduce the experimental behavior of the lasers. There is one caveat: at very low prepulse energies, discrepancies do occur. It is thought that this is most likely a problem of the initial interaction between the laser pulse and solid target, which is currently dealt with in a crude fashion using an energy dump to the outermost cells. We have shown agreement between trends and measured energies for experiment and simulation which, in the past can and have provided a useful aid to experimental design.

ACKNOWLEDGMENTS

The authors wish to thank the other members of the UK x-ray laser consortium for providing detailed data on experimental parameters that have been used in this paper; in particular, A. G. MacPhee, R. Smith, and J. Lin. Thanks are also due to S. Healey, R. King, and S. Maxon for helpful dicussions, suggestions, and advice concerning the data used in the simulations. This research is funded by the United Kingdom Engineering and Physical Sciences Research Council.

---

[1] P.B. Holden, S.B. Healey, M.T.M. Lightbody, G.J. Pert, J.A. Plowes, A.E. Kingston, E. Robertson, C.L.S. Lewis, and D. Neely, J. Phys. B **27**, 341 (1994).

[2] P.L. Hagelstein, Phys. Rev. A **34**, 874 (1986).

[3] W.H. Goldstein, J. Oreg, A. Zigler, A. Bar-Shalom, and M. Klapisch, Phys. Rev. A **38**, 1797 (1988).

[4] S. Maxon (private communication).

[5] H.L. Zhang, D.H. Sampson, and J.F. Fontes, At. Data Nucl. Data Tables **48**, 91 (1991).

[6] J. van Regemorter, Astrophys. J. **136**, 906 (1962).

[7] H. Daido, S. Ninomiya, T. Imani, Y. Okaichi, M. Takagi, R. Kodama, H. Takabe, Y. Kato, F. Koike, J. Nilsen, and K. Murai, Int. J. Mod. Phys. B **11**, 945 (1997).

[8] W.L. van Wyngaarden, K. Bhadra, and R.J.W. Henry, Phys. Rev. A **20**, 1409 (1979).

[9] G.J. Pert, J. Fluid Mech. **131**, 401 (1983).

[10] J.A. Plowes, Opt. Quantum Electron. **28**, 189 (1996).

[11] S. Maxon, K.G. Estabrrok, M.K. Prasad, A.L. Osterheld, R.A. London, and D.C. Eder, Phys. Rev. Lett. **70**, 2285 (1993).

[12] Yu.V. Afansiev, V.N. Shlyaptsev, Kvant. Elektron. (Moscow) **16**, 2499 (1989) [Sov. J. Quantum Electron. **19**, 1606 (1989)].

[13] J. Dunn, A.L. Osterheld, R. Shepherd, W.E. White, V.N. Shlyaptsev, and R.E. Stewart, Phys. Rev. Lett. **80**, 2825 (1998).

[14] P.A. Simms, S. McCabe, G.J. Pert, Opt. Commun. **153**, 164 (1998).

[15] G.J. Pert, J. Phys. B **12**, 2067 (1979).

[16] G.J. Pert, J. Comput. Phys. **39**, 251 (1981).

[17] D.H. Sampson and H.L. Zhang, Phys. Rev. A **45**, 1556 (1991).

[18] I.P. Grant, B.J. McKenzie, P.H. Norrington, D.F. Mayers, and N.C. Pyper, Comput. Phys. Commun. **21**, 207 (1980).

[19] H.R. Griem, *Plasma Spectroscopy* (Mcbran-Hill, New York, 1964).

[20] A.K. Dave, Ph.D. thesis, University of Hull, 1984.

[21] A. MacPhee (private communication).

[22] J.Y. Lin, G.J. Tallents, A.G. MacPhee, R. Smith, E. Wolfrum, J. Zhang, G. Eker, R. Keenan, C.L.S. Lewis, D. Neely, R.M.N. O'Rourke, G.J. Pert, S.J. Pestehe, and J.S. Wark, J. Appl. Phys. **85**, 672 (1999).

[23] G.F. Cairns, S.B. Healy, C.L.S. Lewis, G.J. Pert, and E. Robertson, J. Phys. B **29**, 4839 (1996).

[24] J.Y. Lin, G.J. Tallents, A.G. MacPhee, A. Demir, C.L.S. Lewis, D. Neely, R.M.N. O'Rourke, G.J. Pert, D. Ros, and P. Zeitoun, Opt. Commun. **166**, 211 (1999).